Direct measurement of emittance using the MICE scintillating fibre tracker

V. Blackmore, K. Long

The Muon Ionization Cooling Experiment (MICE) collaboration seeks to demonstrate the feasibility of ionization cooling, the technique by which it is proposed to cool the muon beam at a future neutrino factory or muon collider. The muon beam emittance is derived from an ensemble of muons assembled from muons that pass through the experiment. A pure muon beam is selected using a particle identification system that can reject efficiently both pions and electrons. The position and momentum of each muon is measured using a high-precision scintillating-fibre tracker in a 4 T solenoidal magnetic field. This paper discusses the techniques used to reconstruct the emittance of the muon beam in the upstream spectrometer and reports the emittance of the muon beam as a function of muon-beam momentum.

1 Introduction

Stored muon beams have been proposed as the source of neutrinos at a neutrino factory [1, 2] and as the means to deliver multi-TeV lepton-antilepton collisions at a muon collider [3, 4]. In such facilities the muon beam is produced from the decay of pions generated by a high-power proton beam striking a target. The tertiary muon beam occupies a large volume in phase space. To optimise the muon yield for a neutrino factory, and luminosity for a muon collider, while maintaining a suitably small aperture in the muon-acceleration system requires that the muon beam be "cooled" (i.e., its phase-space volume reduced) prior to acceleration.

A muon is short-lived, with a lifetime of $2.2\,\mu$s in its rest frame. Therefore, beam manipulation at low energy ($\leq 1\,$GeV) must be carried out rapidly. Four cooling techniques are in use at particle accelerators: synchrotron-radiation cooling [5]; laser cooling [6–8]; stochastic cooling [9]; and electron cooling [10]. In each case, the time taken to cool the beam is long compared to the muon lifetime. In contrast, the cooling time associated with ionization cooling, in which the energy of a muon beam is reduced as it passes through a material, the absorber, and is subsequently accelerated, is short enough to allow the muon beam to be cooled efficiently with modest decay losses. Ionization cooling is therefore the technique by which it is proposed to increase the linear current density, for a neutrino factory, and phase-space density for a muon collider [11–13]. This technique has never been demonstrated experimentally and such a demonstration is essential for the development of future high-brightness muon accelerators.

The international Muon Ionization Cooling Experiment (MICE) has been designed [?] to perform a full demonstration of transverse ionization cooling. Intensity effects are negligible for most of the cooling channel conceived for the neutrino factory or muon collider [?]. This allows the MICE experiment to record muon trajectories one particle at a time. The MICE collaboration has constructed two solenoidal spectrometers, one placed upstream, the other downstream, of the cooling cell. An ensemble of muon trajectories is assembled offline, selecting an initial distribution based on quantities measured in the upstream particle identification detectors and upstream spectrometer. This paper describes the techniques used to reconstruct emittance in the spectrometers and presents a measurement of emittance of a variety of momentum-selected beams in the upstream spectrometer.

2 Calculation of emittance

Emittance is a key parameter in assessing the overall performance of an accelerator. The luminosity achieved by a collider is inversely proportional to the beam emittance [?], and therefore small emittance beams are highly desirable.

A beam travelling through a portion of an accelerator may be described in terms of an ensemble of particles. Consider a beam that propagates in the positive z direction of a right-handed Cartesian coordinate system, (x, y, z). The position of the ith particle in the ensemble, $\mathbf{r}_i = (x_i, y_i)$, and its momentum, $\mathbf{p}_i = (p_{xi}, p_{yi})$, then define the coordinates of the particle in transverse phase space. The normalised transverse emittance, ε_N, of the ensemble is the volume occupied by the ensemble of particles in four-dimensional phase space and is given by,

$$\varepsilon_N = \frac{1}{m_\mu} \sqrt[4]{\det \mathcal{C}} \; ; \tag{1}$$

where m_μ is the rest mass of the muon, $\mathcal{C}$ is the four-dimensional covariance matrix defined by:

$$\mathcal{C} = \begin{pmatrix} \sigma_{xx} & \sigma_{xp_x} & \sigma_{xy} & \sigma_{xp_y} \\ \sigma_{xp_x} & \sigma_{p_xp_x} & \sigma_{yp_x} & \sigma_{p_xp_y} \\ \sigma_{xy} & \sigma_{yp_x} & \sigma_{yy} & \sigma_{yp_y} \\ \sigma_{xp_y} & \sigma_{p_xp_y} & \sigma_{yp_y} & \sigma_{p_yp_y} \end{pmatrix} \; ; \tag{2}$$

and:

$$\sigma_{\alpha\beta} = \frac{\left(\Sigma_i^N \alpha_i \beta_i\right) - \left(\Sigma_i^N \alpha_i\right)\left(\Sigma_i^N \beta_i\right)}{N} \; . \tag{3}$$

The MICE experiment is operated such that muons pass through the experiment one at a time. The phase-space coordinates of each muon are measured and an ensemble of muons that is representative of the muon beam is assembled using the measured coordinates upstream of the cooling channel. The normalised transverse emittance of the ensemble is then calculated by evaluating the sums necessary to construct the covariance matrix $\mathcal{C}$ and the normalised transverse emittance is calculated using equation 1.

3 The Muon Ionization Cooling Experiment

The muons for MICE come from the decay of pions produced by an internal target dipping directly into the circulating proton beam in the ISIS synchrotron at the Rutherford Appleton Laboratory (RAL) [14, 15]. The burst of particles resulting from one target dip is referred to as a "spill". A transfer line of 9 quadrupoles, 2 dipoles and a superconducting "decay solenoid" selects a momentum and transports the beam into the experiment [16]. The small fraction of pions that remain in the beam are rejected during analysis using the time-of-flight hodoscopes and Cherenkov counters that are installed in the transfer line upstream of the experiment [17]. A diffuser is installed at the upstream end of the experiment to vary the initial emittance of the beam.

A schematic diagram of the experiment is shown in figure 1. It contains an absorber/focus-coil module sandwiched between two spectrometer-solenoid modules that provide a uniform magnetic field for particle measurement. The focus-coil module has two separate windings that can be operated with the same, or opposed, polarity. A lithium-hydride or liquid-hydrogen absorber can be placed at the centre of the focus-coil module.

The emittance is measured upstream and downstream of the absorber and focus-coil using scintillating-fibre tracking detectors [21] immersed in the solenoid field provided by three superconducting coils (E1, C, E2). The trackers are used to reconstruct the trajectories of individual muons at the entrance and exit of the absorber. The reconstructed tracks are combined with information from instrumentation upstream and downstream of the spectrometer modules to measure the muon-beam emittance at the upstream and downstream tracker reference planes, the surface closest to the absorber. The instrumentation up- and downstream of the spectrometer
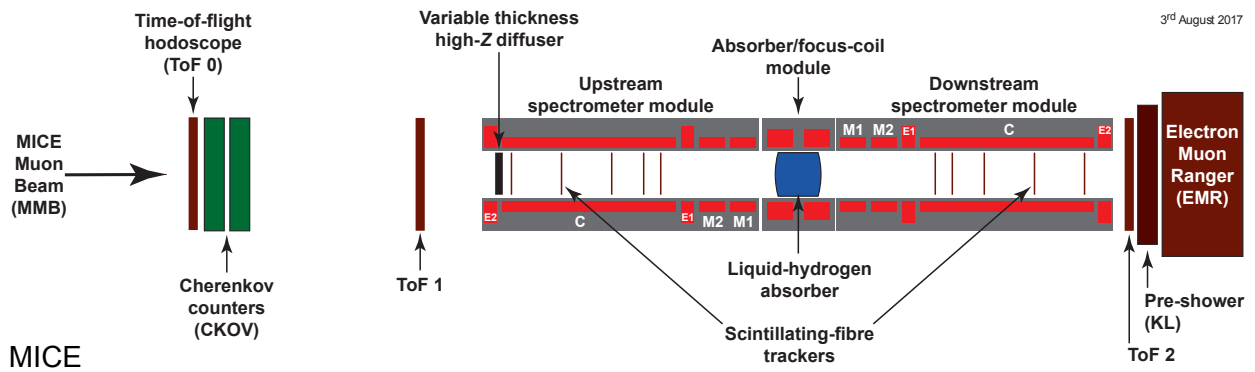
Figure 1: Schematic diagram of the configuration of the experiment. The red rectangles represent the coils of the spectrometer solenoids. The individual coils are labelled E1, C, E2, M1 and M2. The various detectors (time-of-flight hodoscopes [18, 19], Cerenkov counters [20], scintillating-fibre trackers [21], KLOE Light (KL) calorimeter [22?], electron muon ranger [23]) used to characterise the beam are also represented.
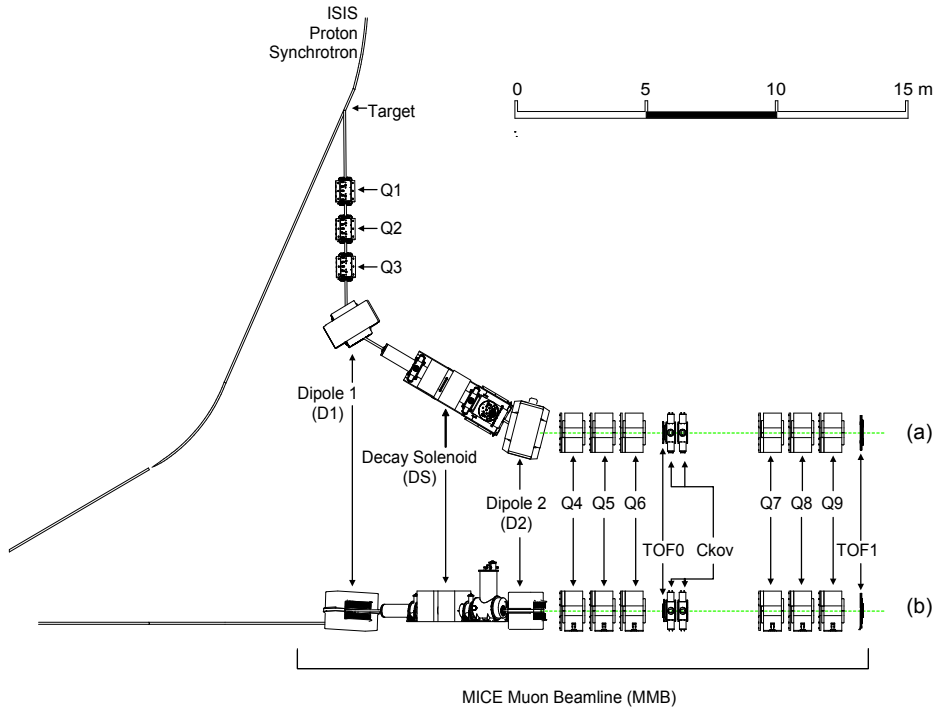
Figure 2: (a) Top and (b) side views of the MICE Transfer Line and its instrumentation. A titanium target dips into the ISIS Proton Synchrotron and the resultant spill of particles is captured with a quadrupole triplet (Q1–3) and transported through momentum-selecting dipoles (D1, D2). The final quadrupole triplets (Q4–6, Q7–9) transport particles to the upstream spectrometer module. The time-of-flight of particles is measured at between ToF0 and ToF1. The time-of-flight is used for particle identification.

modules is used to select a pure sample of muons. The spectrometer-solenoid modules also contain two super-conducting "matching" coils (M1, M2) that are used to match the optics between the solenoid field region and the neighbouring focus-coil.

4   MICE Muon Transfer Line

The MICE Muon Transfer Line, shown schematically in figure 2, is capable of delivering beams with normalised transverse emittance in the range $3 \leq \varepsilon_N \leq 10\pi \, \text{mm} \cdot \text{rad}$ and mean momentum in the range $140 \leq p_\mu \leq 240 \, \text{MeV}/c$ with a root-mean-squared (RMS) momentum spread of $\sim 20 \, \text{MeV}/c$ [16], after a "diffuser" (figure 1). The pneumatically operated diffuser, consisting of tungsten and brass irises of various thicknesses, is at the entrance to the upstream spectrometer module to generate the required emittance range.

Pions produced by the momentary insertion of a titanium target [14, 15] into the 800 MeV ISIS proton beam are captured using a quadrupole triplet (Q1–3) and transported to a first dipole magnet (D1), which selects particles of a desired momentum bite into the 5 T decay solenoid (DS). Muons produced in pion decay in the DS are momentum-selected using a second dipole magnet (D2) and focused onto the diffuser by a quadrupole channel (Q4–6 and Q7–9). In positive-beam running, a borated polyethylene absorber of variable thickness is inserted into the beam just downstream of the DS in order to suppress the high rate of protons that are produced at the target [24].

4

The composition and momentum spectra of the beams delivered to MICE are determined by the interplay between the two bending magnets D1 and D2. In "muon" mode, D2 is set to half the current of D1, selecting backward-going muons in the pion rest frame and producing an almost pure muon beam. The nominal values of the beam momenta, p_μ, are those evaluated at the centre of the absorber, taking into account the energy lost by the particles along the muon beam in the TOF and Cherenkov detectors, the proton absorber (for positive polarity beams), the diffuser and the air along the particle trajectories. For example, a momentum at D2, $p_{\mathrm{D2}} = 238\,\mathrm{MeV}/c$, implies a momentum value $p_\mu = 200\,\mathrm{MeV}/c$ at the centre of the absorber.

Data were taken in October 2015 in muon mode at a nominal momentum of 200 MeV/c. To characterise the properties of the beam accepted by the upstream solenoid, all diffuser irises were withdrawn from the beam. The upstream E1-C-E2 coils in the spectrometer module were energised and produced a 4 T uniform field across the tracking region, while all other coils were unpowered.

5   Simulation

Monte Carlo simulations were used to determine the accuracy of the kinematic reconstruction, to evaluate the efficiency for of the response of the scintillating-fibre tracker, and to study systematic uncertainties. A sufficient number of events was generated to ensure that statistical uncertainties from the simulations were negligible in comparison to those of the data.

The beam impinging on ToF0 was simulated using G4beamline [?]. Particles are produced at the target using a parameterised production model assuming 800 MeV/c operation of the ISIS proton synchrotron[1]. These particles were tracked through the MICE Muon Transfer Line taking into account all material in and surrounding the beam line and using realistic models of the field and apertures of the various magnets. The G4beamline-simulation was tuned to reproduce the observed particle distributions at ToF0.

The MICE User Analysis Software (MAUS) [?] package was used to simulate the passage of particles from ToF0 through the remainder of the transfer line to the solenoidal lattice. This simulation includes the response of the instrumentation, and used the input distribution simulated using G4beamline. In addition to simulation, MAUS also provides a framework for data analysis. MAUS is used for offline analysis and to provide fast real-time detector reconstruction and data visualisation during MICE running. MAUS uses GEANT4 [25, 26] for beam propagation and the simulation of detector response. The events generated were subjected to the same trigger requirements as the data and processed by the same reconstruction programs. ROOT [27] is used for data visualisation and for data storage.

6   Beam selection

The experiment is read out at the end of each spill. This makes it necessary to buffer digital information related to the passage of the particles through the experiment in the front-end electronics (for a description of the MICE trigger and data-acquisition system see [?]). For the reconstructed data presented here, the digitisation of the analogue signals received from the detectors was triggered by a coincidence of signals in the two PMTs serving a single scintillator slab in TOF1. Any slab in TOF1 could generate a trigger.

The following cuts were used to select muons passing through the upstream tracker:

- *One reconstructed space-point in TOF0 and TOF1*: Each TOF hodoscope is composed of two perpendicular planes of scintillator slabs arranged to measure the x and y coordinates. A space-point is formed from the intersection of hits in the x and y projections. Figure 3 shows hit multiplicity in TOF0 plotted against the hit multiplicity in TOF1. The sample is dominated by events with one space-point in both

---

[1]Due to machine issues, ISIS operated at 700 MeV/c in October 2015

Table 1: The number of particles that pass each selection criteria. A total of 24 645 particles pass all of the described cuts.

Cut	No. surviving particles
None	53 276
One space-point in TOF0 and TOF1	37 619
Time of flight in range 27—32 ns	36 357
Single reconstructed track with $\frac{\chi^2}{N_{\mathrm{DOF}}} \leq 4$	40 110
Track within fiducial volume of tracker	52 039
Tracked radius at diffuser $\leq$ 90 mm	42 584
Muon hypothesis	34 121
All	24 645

TOF0 and TOF1. This cut removes events in which two particles enter the experiment within the trigger window;

- *Time of flight between TOF0 and TOF1, t_{01}, in the range $27 \leq t_{01} \leq 32\,ns$*: Figure 3 shows the time of flight distribution for muons passing all cuts other than the time-of-flight cut. The cut on t_{01} removes positrons and a small number of pions that contribute to the sample at large t_{01};

- *A single track reconstructed in the upstream tracker with a track-fit χ^2 satisfying $\frac{\chi^2}{N_{\mathrm{DOF}}} \leq 4$:* N_{DOF} is the number of degrees of freedom. The distribution of $\frac{\chi^2}{N_{\mathrm{DOF}}}$ is shown in figure 3. This cut removes events with poorly reconstructed tracks. In rare cases, more than one particle may pass through the same pixel in TOF0 and TOF1 during the trigger window. This cut removes such events;

- *Track contained within the fiducial volume of the tracker*: The active area of each tracker station extends to a radius of 150 mm. The radius of the track at each tracker station, R_{stn}, is required to satisfy $R_{\mathrm{stn}} < 150$ mm. To ensure the track does not leave and then re-enter the fiducial volume, the track radius is evaluated at 1 mm intervals between the stations. If the track radius exceeds 150 mm at any of these positions, the event is rejected; and

- *Track radius at the diffuser, $R_{\mathrm{diff}} \leq 90\,mm$*: Muons that pass through the material of the diffuser, which includes the retracted irises, lose a substantial amount of energy. Such muons may re-enter the tracking volume and be reconstructed but have properties that are no longer characteristic of the incident muon beam. The inner radius of the diffuser mechanism (100 mm) defines the transverse acceptance of the beam injected into the experiment. Back-extrapolation of tracks to the exit of the diffuser yields a measurement of R_{diff} with a resolution of $\sigma_{R_{\mathrm{diff}}} = 1.8$ mm. Figure 3 shows the distribution of R_{diff}. The cut on R_{diff} accepts particles that passed within $5\sigma_{R_{\mathrm{diff}}}$ of the inner radius of the diffuser.

A total of 24 645 events pass the cuts listed above (Table 1). Data distributions are compared to the distributions obtained using the MAUS simulation in figure 3. The distribution of the time of flight between TOF0 and TOF1 is peaked towards slightly longer times in the simulation than in the data. This is related to the imperfect simulation of the distribution of longitudinal momentum of particles in the beam (see below). The distribution of $\frac{\chi^2}{N_{\mathrm{DOF}}}$ is broader and peaked at slightly larger values in the data than in the simulation. Despite these minor disagreements, the agreement between the simulation and data is sufficiently good to give confidence that a clean sample of muons is selected. Table 2 shows the proportions of surviving positrons, muons, and pions in the MAUS simulation. The expected pion contamination in the unselected ensemble of particles is 0.4%. The criteria used to select the analysed ensemble remove all electrons and pions from the Monte Carlo sample.

Figure 4 shows t_{01} plotted as a function of p, the momentum reconstructed by the upstream tracking detector. The same distribution obtained from the simulation is also shown. The bulk of the data is consistent with
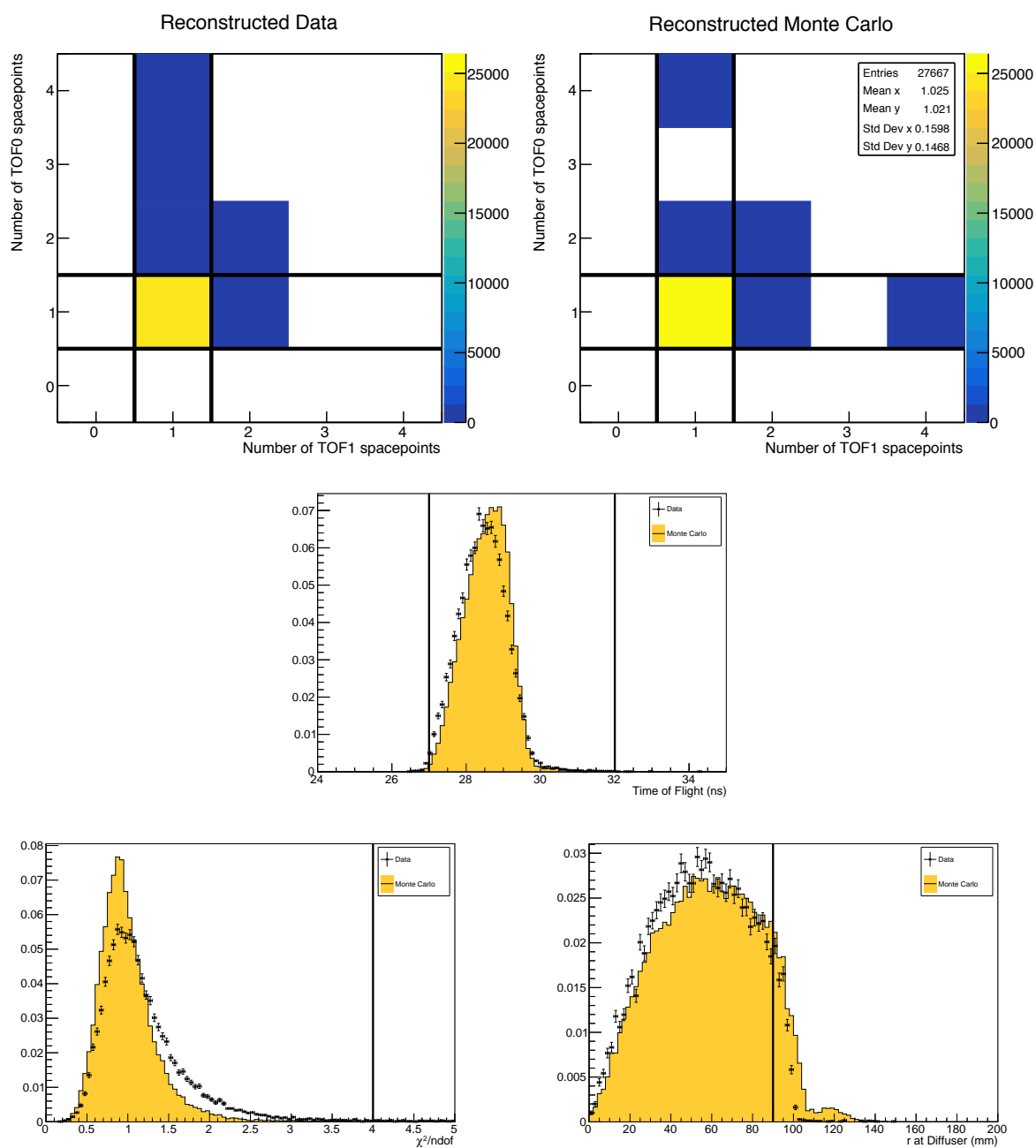
Figure 3:   Distribution of the quantities used to select the sample used to reconstruct the emittance of the beam. Top: the number of space-points in TOF0 plotted against the number of space-points in TOF1; Middle: distribution of t_{01}; Bottom left: distribution of $\frac{\chi^2}{N_{\mathrm{DOF}}}$; and Bottom right: distribution of R_{diff}. In each case the data is shown as the solid circles or, in the case of the space-point distributions in TOF1 and TOF0, the black squares and the distribution obtained with the MAUS simulation is shown as the solid yellow histogram. The solid black lines indicate the position of the cuts made on the various quantities. Events enter the plots if all cuts other than the cut under examination are passed.

Table 2: The proportion of electrons, muons, and pions, at the upstream Tracker, that survive each cut in the Monte Carlo simulation. Application of all cuts removes all electrons and pions in the reconstructed Monte Carlo sample.

Cut	e	μ	π	Total
None	1 676	46 113	203	47 992
One space-point in TOF0 and TOF1	1 275	37 574	151	40 015
Time of flight in range 27—32 ns	71	39 267	152	40 322
Single reconstructed track with $\frac{\chi^2}{N_{\mathrm{DOF}}} \leq 4$	1 205	43 824	163	45 194
Track within fiducial volume of tracker	1 641	43 903	175	45 719
Tracked radius at diffuser $\leq$ 90 mm	1 332	32 270	112	33 714
Muon hypothesis	298	38 285	40	38 630
All	0	26 414	0	26 414

the muon hypothesis, depicted by the dashed (white) line. Events lying above the upper black (solid) lines in figure 4 are ascribed to the passage of pions and are removed from the analysis. The population of events lying below the lower solid-black line arise from muons that are poorly reconstructed or have passed through support material upstream of the tracker and lost momentum. These muons are also removed from the analysis. 19 153 events are removed by this requirement.

7 Results

7.1 Phase-space projections

The distributions in $x, y, p_x, p_y, p_z, p_\perp^2, p_\perp$ (where $p_\perp^2 = p_x^2 + p_y^2$), and $p = \sqrt{p_x^2 + p_y^2 + p_z^2}$ are shown in figure 5. The distributions are plotted at the reference surface of the upstream tracker; the most downstream surface of the scintillating-fibre plane closest to the absorber/focus-coil module. The total momentum of the muons that make up the beam lie within the range $140 \lesssim |p| \lesssim 260$ MeV/c. The results of the MAUS simulation, which are also shown in figure 5, give a good description of the data. In the case of the longitudinal component of momentum, p_z, the data is peaked to slightly larger values than the simulation. The difference is small and is reflected in the distribution of the total momentum, p. The distributions of the components of the transverse phase space (x, p_x, y, p_y) are well described by the simulation.

The phase space occupied by the beam selected by the procedure described in section 6 is shown in figure 6. The distributions are plotted at the reference surface of the upstream tracker. The beam is well centred in the (x, y) plane. Correlations are apparent that couple the position and momentum components in the transverse plane. The transverse position and momentum coordinates are also seen to be correlated with longitudinal momentum. The dispersion in the beam is discussed further in section 7.2.

7.2 Dispersion and binning in longitudinal momentum

Momentum selection at D2 introduces a correlation between position and momentum. Figure 7 shows the transverse positions and momenta with respect to the longitudinal momentum, p_z, as measured at the upstream Tracker reference plane. Correlations exist between all four transverse phase-space co-ordinates and the longitudinal momentum.
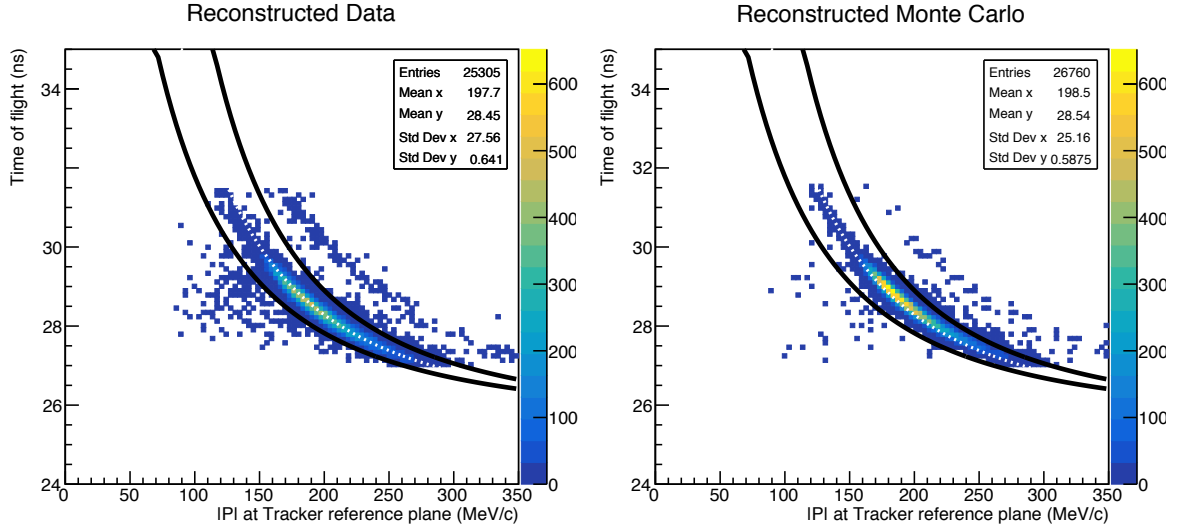
Figure 4: Time of flight between TOF0 and TOF1 (t_{01}) plotted as a function of the muon momentum, p, measured in the upstream tracker. Particles within the black lines are selected as a pure muon sample. The (white) dotted line is the trajectory of a muon that loses the mean momentum (20 MeV/c) between TOF1 and the tracker. (Left) Reconstructed Data, (Right) Reconstructed Monte Carlo.
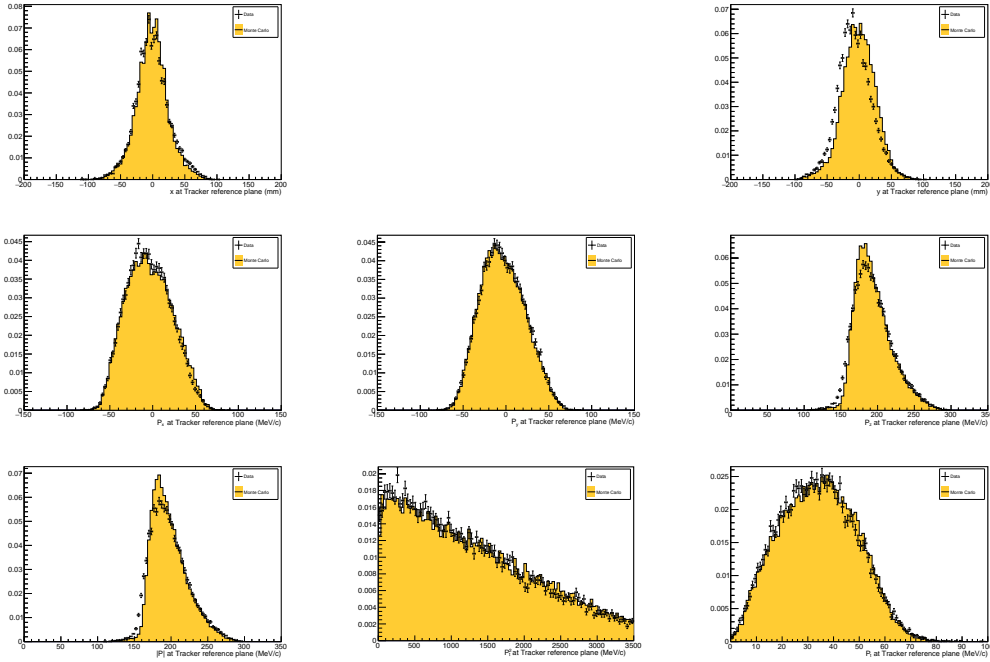

Figure 5: Position and momentum distributions of muons reconstructed at the reference surface of the upstream tracker. The top left and top right panels show the distributions of x and y respectively. The distributions of components of the muon momentum are shown in the middle row; p_x in the left-middle panel, p_y in the centre middle panel and p_z in the right-middle panel. The distribution of the total momentum, p, is shown in the bottom-left panel. The distributions of the transverse momentum squared, $p_{\perp}^2 = p_x^2 + p_y^2$, and $p_{\perp}$ are shown in the bottom-middle and bottom-right panels respectively. The data is shown as the solid circles while the results of the MAUS simulation are shown as the yellow histogram.
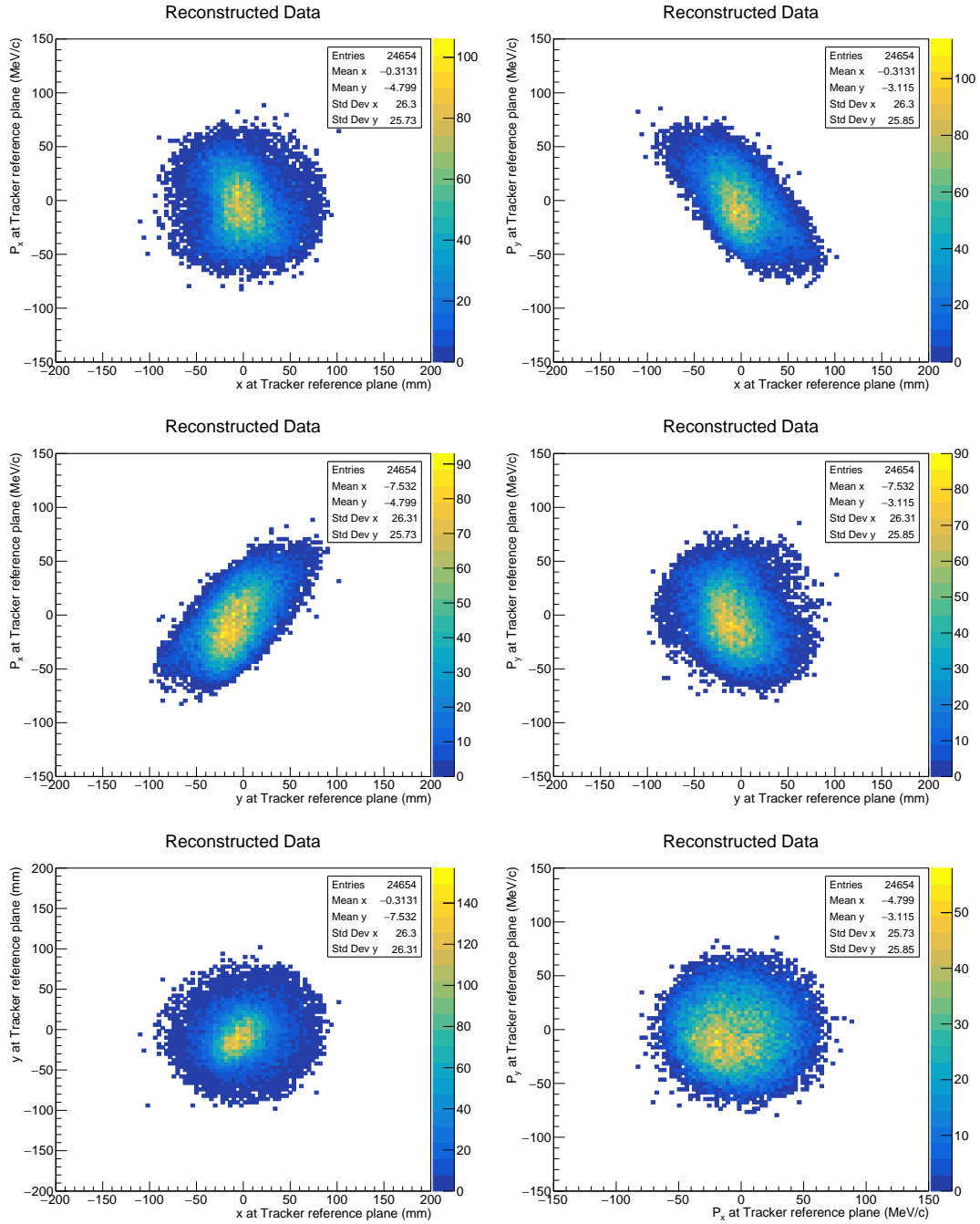
9

Figure 6: Transverse phase space occupied by selected muons transported through the MICE Muon Transfer Line to the reference plane of the upstream Tracker. Top left: (x, p_x), top right: (x, p_y). Middle left: (y, p_x), middle right: (y, p_y). Bottom left: (x, y), bottom right: (p_x, p_y).
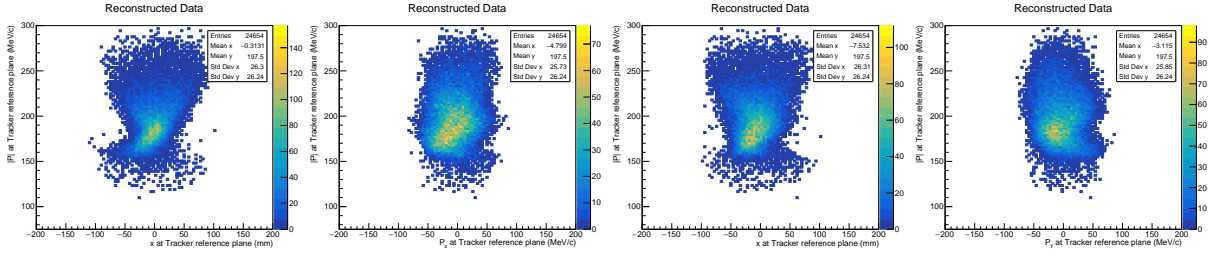
10

Figure 7: Momentum selection at D2 introduces correlations between position and momentum. Dispersion is shown, from left to right, in x, p_x, y, and p_y, with respect to the longitudinal momentum, p_z, measured at the upstream Tracker reference plane.
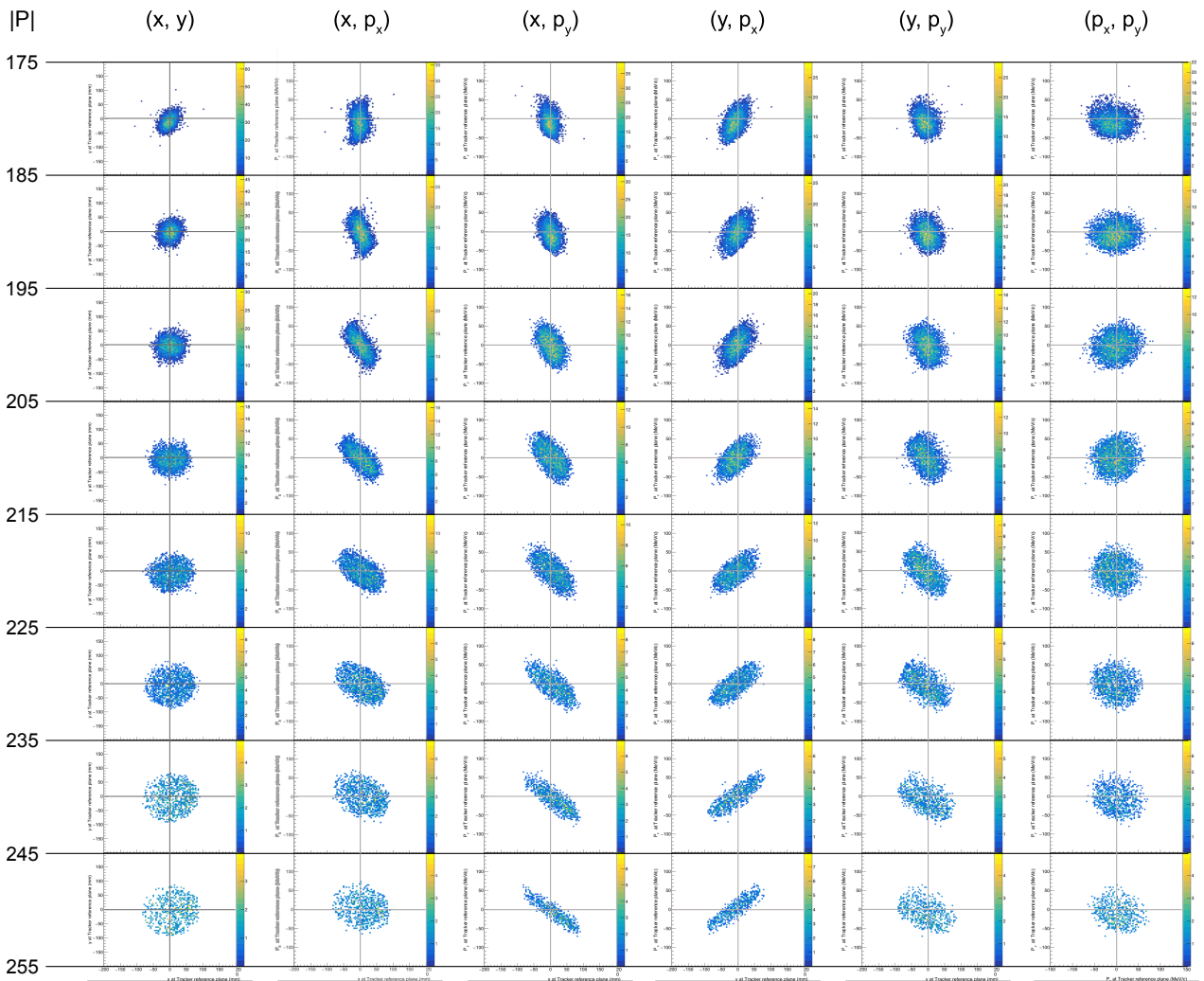

Figure 8: Phase-space distributions binned in $10\,\mathrm{MeV}/c$ increments of total momentum, p. The orientation of the phase-space projections is momentum-dependent. The emittance of each momentum bin is reported in table 3. The axis arrangement and scale of each phase-space projection are as in the equivalent figure showing particles of all momenta, figure 6.
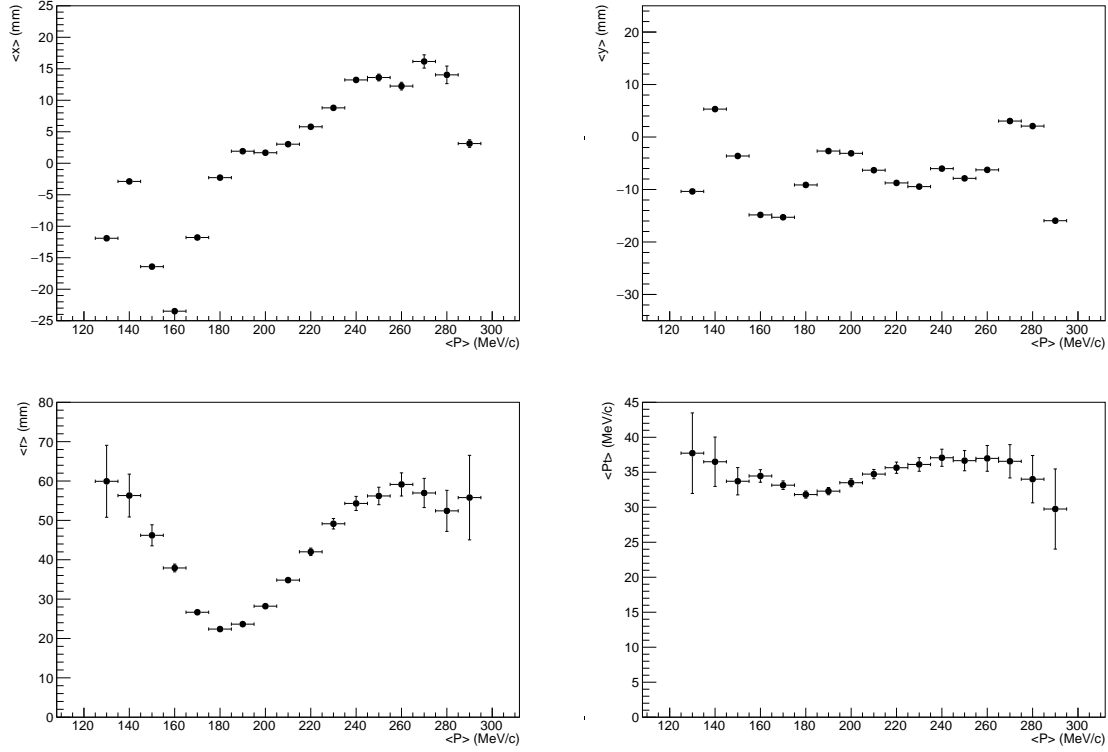
Figure 9: Variation in mean particle parameters as a function of p. Top left: x, top right: y, bottom left: mean track radius, r, bottom right: mean $p_\perp$.

The momentum-dependence of the orientation of the phase-space projections is clearly seen in figure 8. The ensemble shown in figure 6 is divided into $10\,\mathrm{MeV}/c$ bins of total momentum, p. As p increases, the phase space volume occupied by the beam rotates. The emittance of each sub-division is calculated separately to account for this optical mismatch.

Figure 9 shows the mean x, y of the muon beam as a function of p in $10\,\mathrm{MeV}/c$ p bins. The mean horizontal position systematically shifts to positive x as the momentum of the sample increases above $175\,\mathrm{MeV}/c$. The variation seen in the mean vertical position is due to the helical trajectory particles take coupled with the offset horizontal position of the particles when entering the solenoid field. The mean radial position r ($r = \sqrt{x^2 + y^2}$) is also shown as a function of p. The mean r increases as p increases above $175\,\mathrm{MeV}/c$, reflecting the increase in the mean x with p. The mean $p_\perp$ is plotted as a function of p in figure 9. For p greater than $\approx 175\,\mathrm{MeV}/c$, the mean $p_\perp$ rises with increasing p. For $p \lesssim 175\,\mathrm{MeV}/c$, the mean $p_\perp$ rises rapidly as p falls. The dependence of the mean $p_\perp$ on p for $p < 175\,\mathrm{MeV}/c$ is related to the negative correlation between p_y and p for values of p below $175\,\mathrm{MeV}/c$ (see figure 6).

The kinematic region over which the emittance has been determined is $175 \leq p \leq 255\,\mathrm{MeV}/c$ since the dependence of the mean $p_\perp$ on p_z changes qualitatively for $p \lesssim 175\,\mathrm{MeV}/c$ and the beam contains relatively few events with $p \gtrsim 260\,\mathrm{MeV}/c$. Beyond this region, the beam falls outside the acceptance of the upstream solenoid and is scraped. The size of the bins of p used to report the reconstructed emittance were chosen commensurate with the resolution. The p resolution is plotted as a function of p in figure 10. The resolution in p (σ_p) varies from $\sim$??? MeV/c for $p \leq 160\,\mathrm{MeV}/c$ and rises linearly from $\sim$??? MeV/c at $160\,\mathrm{MeV}/c$ to $\sim$??? MeV/c at ??? MeV/c. A bin width of $10\,\mathrm{MeV}/c$ was therefore chosen. The number of events per bin is shown in figure 11. The number of events per bin varies from $\sim 4\,000$ for $p \sim 180\,\mathrm{MeV}/c$ to ~ 900 for
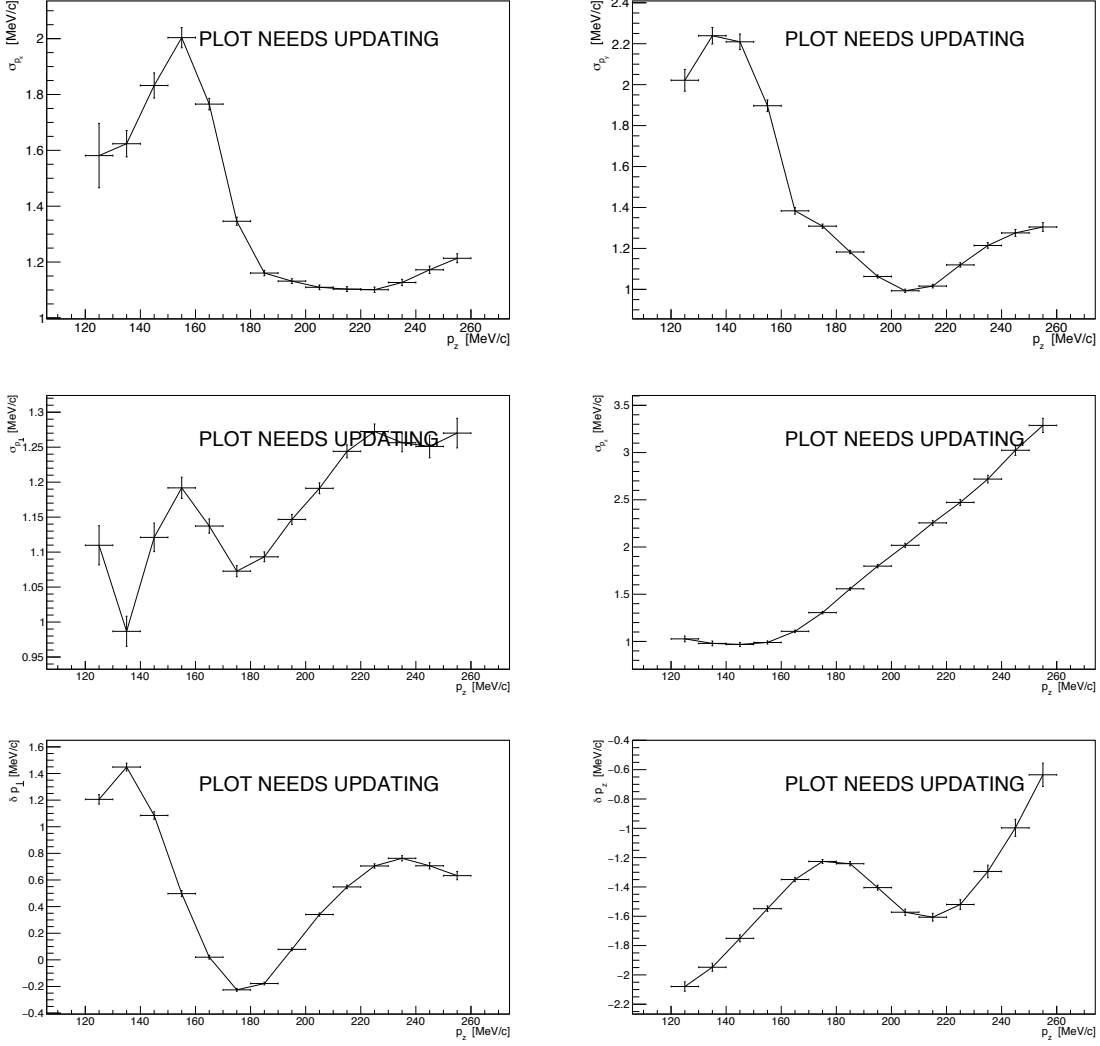
12

Figure 10: Resolution and bias of reconstructed track parameters as a function of p_z. Top left: Reconstruction resolution on p_x, top right: p_y, middle left: $p_\perp$, middle right: p_z. Bottom left: Reconstruction bias on $p_\perp$, bottom right: p_z.

$p \sim 250$ MeV/c. The efficiency, η, and purity, ζ, of the selected ensemble are defined as,

$$\eta = \frac{N_c}{N_G}, \tag{4}$$

$$\zeta = \frac{N_c}{N_R}, \tag{5}$$

where, for a specific momentum bin, N_c is the total number of generated and reconstructed events that survive the selection criteria (Section 6), N_G is the number of events generated in that bin, and N_R is the number of events reconstructed in the bin. The efficiency and purity are always ≈ 1. Figure 11 shows $1 - \eta$ and $1 - \zeta$, showing their deviation from unity.

The reconstructed emittance is a convolution of the true particle distribution and the reconstruction resolutions for each parameter. The tracker reconstruction has a position resolution of approximately 0.34 mm in both x and y, uniform with p_z, while the transverse momentum resolutions are approximately 1.5 MeV/c (see figure 10). Assuming a completely uncorrelated distribution of particles, and Gaussian resolutions, the systematic
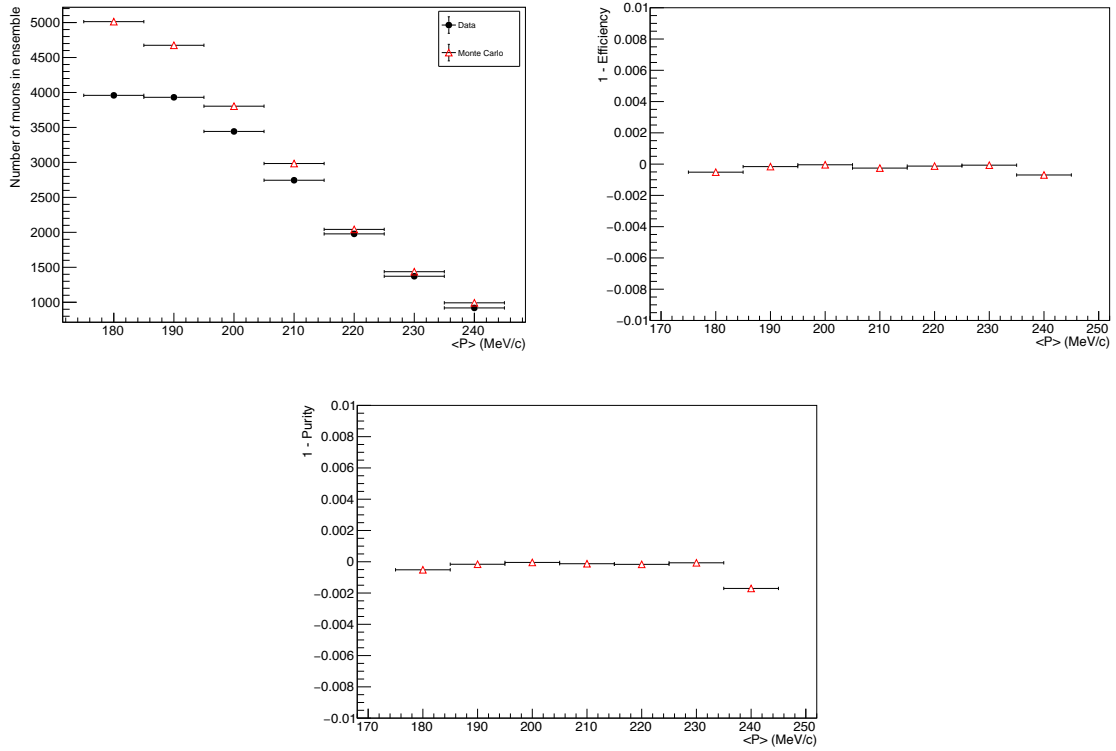
13

Figure 11: Top left: The number of muons in each momentum bin in reconstructed data (black, circle) and reconstructed Monte Carlo (red, triangle). Top right: $1 - \eta$, where η is the reconstructed Monte Carlo selection efficiency, as a function of p. Bottom: $1 - \zeta$, where ζ is the reconstructed Monte Carlo selection purity, as a function of p. Both efficiency and purity are ≈ 1.

correction to the emittance reconstruction can be estimated to be less than 10^{-3}. The presence of correlations within the beam, however increase the significance of the systematic correction. For distributions presented in figure 6 the expected correction is estimated to be small.

The statistical uncertainty on the emittance of each momentum bin is calculated as $\sigma_\epsilon = \frac{\epsilon}{\sqrt{2N}}$ [28], where ϵ is the emittance of the ensemble of muons in the specified momentum range and N is the number of muons in the ensemble.

7.3 Systematic uncertainties

Systematic uncertainties related to the beam selection were estimated by varying the cut values by an amount corresponding to the RMS resolution of the quantity in question. Systematic uncertainties related to possible biases in calibration constants were evaluated by varying the calibration constant in line with its resolution. Systematic uncertainties related to the reconstruction algorithms were evaluated using the MAUS simulation. The positive and negative deviations from the nominal emittance were added in quadrature separately to obtain the total positive and negative systematic uncertainly. Sources of uncorrelated and correlated uncertainties are discussed in detail below.

7.3.1 Uncorrelated systematic uncertainties

Systematic uncertainties related to beam selection have been estimated by varying the cut values according to the RMS resolution of the cut variables. The overall uncertainty due to beam selection is summarised in table 3.

7.3.2 Correlated systematic uncertainties

Systematic uncertainties correlated with p_z are:

- Non-uniform magnetic field across the tracking region gives a bias in $p_\perp$ and p reconstruction. This uncertainty will be evaluated using a MAUS simulation comparing the expected non-uniform field with a uniform field.
- Time-of-flight and track reconstruction are combined to improve reconstruction of tracks with low $p_\perp$. The uncertainty on the time-of-flight is $\sim 70\,\text{ps}$.
- Tracker to field misalignment.
- Field magnitude. A MAUS model will be studied with the modelled (non-uniform) field scaled to the values measured by the Hall probes during the period over which data was taken. The field will be scaled above and below this value by an amount equal to the variation in the Hall probe readings.
- The measured value of p dictates the momentum bin a muon is assigned to for the emittance calculation. The uncertainty on each bin associated with this has been evaluated by allowing each muon's p to fluctuate around its measured value according to a Gaussian of width equal to the measurement uncertainty on p. The uncertainty due to this binning is summarised in table 3.
- Uncertainty on the reconstructed x, p_x, y, p_y and the effect on the calculated emittance was evaluated similarly to the uncertainty on p. The uncertainty due to detector resolution in summarised in table 3.

7.4 Emittance

The measured transverse normalised emittance as a function of p is shown in figure 12 (left). Uncertainties are those summarised in table 3. The emittance of the measured muon ensemble is approximately flat across

15

Table 3: Statistical and systematic uncertainties on the measured emittance as a function of p.

| Source	$\langle p \rangle$ (MeV/c)							
	180	190	200	210	220	230	240	250
Measured emittance (mm rad)	3.06	3.40	3.65	3.69	3.65	3.69	3.62	3.31
Statistical uncertainty	±0.03	±0.04	±0.04	±0.05	±0.05	±0.07	±0.08	±0.09
Beam selection	$^{+0.05}_{-0.04}$	$^{+0.05}_{-0.04}$	$^{+0.06}_{-0.05}$	$^{+0.05}_{-0.06}$	±0.05	$^{+0.04}_{-0.05}$	±0.1	$^{+0.05}_{-0.1}$
Binning in p	±0.02	±0.02	±0.02	±0.02	±0.03	±0.03	±0.04	±0.05
Non-uniform magnetic field	±???	±???	±???	±???	±???	±???	±???	±???
Low $p_\perp$ tracks	±???	±???	±???	±???	±???	±???	±???	±???
Tracker-field misalignment	±???	±???	±???	±???	±???	±???	±???	±???
Magnetic field scale	±???	±???	±???	±???	±???	±???	±???	±???
Tracker resolution	±0.00	±0.00	±0.00	±0.00	±0.00	±0.01	±0.01	±0.01
Total systematic uncertainty	$^{+0.06}_{-0.04}$	$^{+0.06}_{-0.04}$	$^{+0.07}_{-0.05}$	±0.06	±0.06	±0.34	$^{+0.11}_{-0.10}$	$^{+0.07}_{-0.11}$
Total uncertainty	$^{+0.07}_{-0.05}$	$^{+0.06}_{-0.05}$	$^{+0.08}_{-0.07}$	±0.08	±0.08	±0.34	$^{+0.14}_{-0.13}$	$^{+0.12}_{-0.14}$
Total uncertainty (%)	$^{+2.14}_{-1.71}$	$^{+1.98}_{-1.60}$	$^{+2.17}_{-1.85}$	$^{+2.06}_{-2.20}$	$^{+2.29}_{-2.25}$	$^{+9.29}_{-9.31}$	$^{+3.89}_{-3.54}$	$^{+3.49}_{-4.32}$
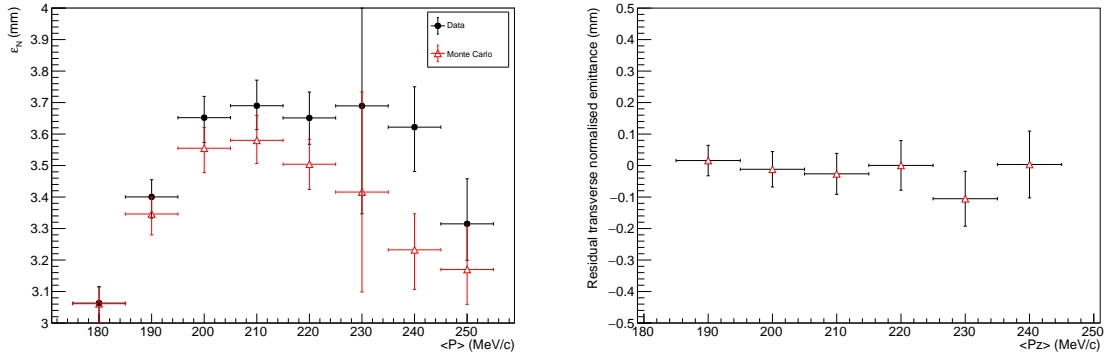
Figure 12: Left: Variation in normalised transverse emittance as a function of p_z for data (black, circle) and reconstructed Monte Carlo (red, triangle). Error bars are statistical. Right: Resolution of emittance reconstruction from Monte Carlo.

the selected momentum range, with the exception of muons between $??? \leq p \leq ???\,\mathrm{MeV}/c$. The emittance of the reconstructed Monte Carlo (red, triangles) is ??? than that of the data (black, circles) and shows a ??? in emittance between $??? \leq p \leq ???\,\mathrm{MeV}/c$, contrary to the data. The mean transverse normalised emittance across the full momentum range is $???\pm???\,\mathrm{mm\,rad}$.

A small bias on the emittance of the reconstructed Monte Carlo is shown in figure 12 (right), which tends to increase with increasing p. There is a similar increase in the emittance bias in the $??? \leq p \leq ???\,\mathrm{MeV}/c$ bin.

8 Conclusions

Still to do:
- Obtain equivalent data and MC datasets using the same reconstruction algorithms, with global track matching to the position of the diffuser (in progress, D. Rajaram);
- generate larger MC data sets so that MC contibution to the statistical error can be negleted (D. Rajaram).
- Check emittance bias (and quantify claim that bias is small made in section 7) with updated MC sample (V. Blackmore)
- Work through systematic error list (V. Blackmore, C. Hunt)
- Update to figure 2 to include Step IV equipment.

References

[1] S. Geer, "Neutrino beams from muon storage rings: Characteristics and physics potential," *Phys. Rev.* **D57** (1998) 6989–6997, `arXiv:hep-ph/9712290`.

[2] M. Apollonio *et al.*, "Oscillation physics with a neutrino factory," `hep-ph/0210192`.

[3] D. V. Neuffer and R. B. Palmer, "A High-Energy High-Luminosity $\mu^+ - \mu^-$ Collider," *Conf. Proc.* **C940627** (1995) 52–54.

[4] R. B. Palmer, "Muon Colliders," *Rev. Accel. Sci. Tech.* **7** (2014) 137–159.

[5] S. Y. Lee, *Accelerator Physics (Third Edition).* World Scientific Publishing Co, 2012.

[6] S. Schröder, R. Klein, N. Boos, M. Gerhard, R. Grieser, G. Huber, A. Karafillidis, M. Krieg, N. Schmidt, T. Kühl, R. Neumann, V. Balykin, M. Grieser, D. Habs, E. Jaeschke, D. Krämer, M. Kristensen, M. Music, W. Petrich, D. Schwalm, P. Sigray, M. Steck, B. Wanner, and A. Wolf, "First laser cooling of relativistic ions in a storage ring," *Phys. Rev. Lett.* **64** (Jun, 1990) 2901–2904. `http://link.aps.org/doi/10.1103/PhysRevLett.64.2901`.

[7] J. S. Hangst, M. Kristensen, J. S. Nielsen, O. Poulsen, J. P. Schiffer, and P. Shi, "Laser cooling of a stored ion beam to 1 mk," *Phys. Rev. Lett.* **67** (Sep, 1991) 1238–1241. `http://link.aps.org/doi/10.1103/PhysRevLett.67.1238`.

[8] P. J. Channell, "Laser cooling of heavy ion beams," *Journal of Applied Physics* **52** no. 6, (1981) 3791–3793, `http://dx.doi.org/10.1063/1.329218`. `http://dx.doi.org/10.1063/1.329218`.

[9] J. Marriner, "Stochastic cooling overview," *Nucl. Instrum. Meth.* **A532** (2004) 11–18, `arXiv:physics/0308044 [physics]`.

[10] V. V. Parkhomchuk and A. N. Skrinsky, "Electron cooling: 35 years of development," *Physics-Uspekhi* **43** no. 5, (2000) 433–452. `http://stacks.iop.org/1063-7869/43/i=5/a=R01`.

[11] A. N. Skrinsky and V. V. Parkhomchuk, "Cooling Methods for Beams of Charged Particles. (In Russian)," *Sov. J. Part. Nucl.* **12** (1981) 223–247. [Fiz. Elem. Chast. Atom. Yadra12,557(1981)].

[12] D. Neuffer, "Principles and Applications of Muon Cooling," *Conf.Proc.* **C830811** (1983) 481.

[13] D. Neuffer, "Principles and Applications of Muon Cooling," *Part. Accel.* **14** (1983) 75–90.

[14] C. N. Booth *et al.*, "The design, construction and performance of the MICE target," *JINST* **8** (2013) P03006, `arXiv:1211.6343 [physics.ins-det]`.

[15] C. N. Booth *et al.*, "The design and performance of an improved target for MICE," *JINST* **11** no. 05, (2016) P05006, `arXiv:1603.07143 [physics.ins-det]`.

[16] **MICE collaboration** Collaboration, M. Bogomilov *et al.*, "The MICE Muon Beam on ISIS and the beam-line instrumentation of the Muon Ionization Cooling Experiment," *JINST* **7** (2012) P05009, `arXiv:1203.4089 [physics.acc-ph]`.

[17] **MICE** Collaboration, D. Adams *et al.*, "Characterisation of the muon beams for the Muon Ionisation Cooling Experiment," *Eur. Phys. J.* **C73** no. 10, (2013) 2582, `arXiv:1306.1509 [physics.acc-ph]`.

18

[18] **Mice Collaboration** Collaboration, R. Bertoni *et al.*, "The design and commissioning of the MICE upstream time-of-flight system," *Nucl.Instrum.Meth.* **A615** (2010) 14–26, `arXiv:1001.4426 [physics.ins-det]`.

[19] R. Bertoni, M. Bonesini, A. de Bari, G. Cecchet, Y. Karadzhov, and R. Mazza, "The construction of the MICE TOF2 detector."
`http://mice.iit.edu/micenotes/public/pdf/MICE0286/MICE0286.pdf`, 2010.

[20] L. Cremaldi, D. A. Sanders, P. Sonnek, D. J. Summers, and J. Reidy, Jr, "A Cherenkov Radiation Detector with High Density Aerogels," *IEEE Trans. Nucl. Sci.* **56** (2009) 1475–1478, `arXiv:0905.3411 [physics.ins-det]`.

[21] M. Ellis *et al.*, "The design, construction and performance of the MICE scintillating fibre trackers," *Nucl. Instrum. Meth.* **A659** (2011) 136–153, `arXiv:1005.3491 [physics.ins-det]`.

[22] F. Ambrosino *et al.*, "Calibration and performances of the KLOE calorimeter," *Nucl. Instrum. Meth.* **A598** (2009) 239–243.

[23] R. Asfandiyarov *et al.*, "The design and construction of the MICE Electron-Muon Ranger," *JINST* **11** no. 10, (2016) T10007, `arXiv:1607.04955 [physics.ins-det]`.

[24] S. Blot, "Proton Contamination Studies in the MICE Muon Beam Line," *Proceedings 2nd International Particle Accelerator Conference (IPAC 11) 4-9 September 2011, San Sebastian, Spain* (2011) .

[25] **GEANT4** Collaboration, S. Agostinelli *et al.*, "Geant4: A simulation toolkit," *Nuclear Instruments and Methods in Physics Research A* **506** (2003) 250–303.

[26] J. Allison *et al.*, "Geant4 developments and applications," *IEEE Trans. Nucl. Sci.* **53** (2006) 270–278.

[27] R. Brun and F. Rademakers, "ROOT: An object oriented data analysis framework," *Nucl. Instrum. Meth.* **A389** (1997) 81–86.

[28] J. H. Cobb, "Statistical errors on emittance," 2015.